ADVANCED BIOLOGY
www.advanced-bio.com

Polymer Nanopillars Induce Increased Paxillin Adhesion Assembly and Promote Axon Growth in Primary Cortical Neurons

*Frano Milos, Andreea Belu, Dirk Mayer, Vanessa Maybeck, and Andreas Offenhäusser**

The complexity of the extracellular matrix consists of micro- and nanoscale structures that influence neuronal development through contact guidance. Substrates with defined topographic cues mimic the complex extracellular environment and can improve the interface between cells and biomedical devices as well as potentially serve as tissue engineering scaffolds. This study investigates axon development and growth of primary cortical neurons on OrmoComp nanopillars of various dimensions. Neuronal somas and neurites form adhesions and F-actin accumulations around the pillars indicating a close contact to the topography. In addition, higher pillars (400 nm) confine the growing neurites, resulting in greater neurite alignment to the topographical pattern compared to lower pillars (100 nm). A comprehensive analysis of growth cone dynamics during axon development shows that nanopillars induce earlier axon establishment and change the periodicity of growth cone dynamics by promoting elongation. This results in longer axons compared to the flat substrate. Finally, the increase in surface area available for growth cone coupling provided by nanopillar sidewalls is correlated with increased assembly of paxillin-rich point contact adhesions and a reduction in actin retrograde flow rates allowing for accelerated and persistent neurite outgrowth.

1. Introduction

In the complex microenvironment of an extracellular matrix (ECM), the crosstalk between different stimuli affects various aspects of physiological[1] and pathological processes.[2] The ECM architecture consists of complex structures ranging from micrometers to nanometers in size that modulate ECM chemistry, topography, stiffness, and frequency of adhesion points. Topographical cues provide local constraints compatible with cellular nanoscale structures (e.g., filopodia) and exert an influence on development, differentiation, and neuritogenesis by providing contact guidance cues.[3] Although many fundamental principles in cell biology have been studied on flat 2D substrates, these oversimplified platforms hardly recapitulate the complexity of in vivo microenvironments.[4]

In the past two decades, advances in micro- and nanotechnology have enabled fabrication of substrates with defined topographies that mimic certain features of the in vivo environment while still maintaining the simplicity and reproducibility of 2D in vitro systems. More recently, the attention has been focused on the investigation of the ECM nanotopography, which strongly influences cellular polarity, migration, proliferation, and differentiation.[5] Nanotopography has been modelled in the form of different arrays containing parallel nanogrooves,[6] nanopillars/holes,[7] fibers,[8] carbon nanotubes,[9] etc. Traditionally, anisotropic microgrooves and ridges were used to study axonal development and guidance but more recently it has been shown that interrupted isotropic features (e.g., holes) are stronger cues for attracting axonal specification.[10] Recently, our group reported that asymmetric poly(dichloro-p-xylene) (PPX) films with dense, inclined nanocolumns enhance neurite branching and axonal elongation. Furthermore, the asymmetric orientation of polymeric nanocolumns provides contact guidance cues and strongly influences axonal initiation direction.[11] Contact guidance has a particular role both in the development of the nervous system[12] and in response to injury in the peripheral nervous system.[13] On the other hand, injuries in the central nervous system are incapable of spontaneous repair due to the formation of physical and chemical barriers and a lack of a prompt immune response.[14] Therefore, a considerable effort is being made to engineer a permissive environment for nerve regeneration by implementing different regeneration scaffolds.[15] Furthermore, topography can be used to improve

F. Milos, Dr. D. Mayer, Dr. V. Maybeck, Prof. A. Offenhäusser
Institute of Biological Information Processing IBI-3
Forschungszentrum Jülich GmbH
Jülich 52425, Germany
E-mail: a.offenhaeusser@fz-juelich.de
F. Milos, Prof. A. Offenhäusser
RWTH Aachen
Aachen, Germany
Dr. A. Belu
Department of Anesthesiology and Intensive Care Medicine
University Hospital of Cologne
Cologne 50931, Germany
The ORCID identification number(s) for the author(s) of this article can be found under https://doi.org/10.1002/adbi.202000248.

DOI: 10.1002/adbi.202000248

devices that interface with neurons in vitro and in vivo by mimicking natural structures, improving adhesion, and reducing the cell-electrode gap.[16,17] Specifically, vertical nanopillars have been used to improve cell adhesion[18] and as electrodes to measure neuronal action potentials.[19,20]

In this study, we used nanopillar arrays to investigate the effects of isotropic topography on adhesion and early development of primary cortical neurons in vitro. A biocompatible polymer OrmoComp was employed to fabricate frustum-shaped nanoscale pillar arrays resulting in a transparent in vitro platform compatible with conventional optical microscopy. We evaluated both neuronal soma adhesion and neurite outgrowth on nanopillar arrays in comparison to flat OrmoComp substrates. Time-lapse microscopy was used to systematically study axonal growth dynamics, including the time until axon establishment, periodicity of growth phases (elongation, pausing, retraction), and the resulting axon length. Finally, the influence of pillar topographies on point contact adhesions and F-actin retrograde flow in the growth cone was analyzed.

2. Results and Discussion

2.1. Topographical Characteristics of OrmoComp Arrays

OrmoComp is a biocompatible organic-ceramic polymer compatible with nanoimprint lithography.[21,22] Topographic patterns were created by fabricating nanostructured molds on Si/SiO_2 substrates (Figure S1, Supporting Information), followed by their replication onto OrmoComp-coated quartz wafers using nanoimprint lithography (Figure S2, Supporting Information). This resulted in a transparent and durable replica and made the fabrication process relatively inexpensive. Topographies consisted of pillars with defined dimensions uniformly ordered along the vertical and horizontal axes in a square lattice. A total of six topographies with different pillar base diameters (500, 750, 1000 nm) and heights (100 and 400 nm) were used (**Table 1**). The pitch of all the arrays was twice their respective diameter (thus 1, 1.5, 2 µm, respectively). Therefore, fabricated arrays had a defined pillar diameter and pitch and a uniform spatial frequency (density) of topographical cues that varied on different arrays. The structures were characterized as conical frustums (Figure S2b,c, Supporting Information) with a frustum angle of ≈115° for 100 nm high pillars and ≈120° for 400 nm high pillars.

Table 1. Dimensions of nanopillars used in the presented study.

Arrays	Diameter [nm][a)]	Pitch [µm]	Height [nm]	Surface area [%][b)]
L500	500	1	100	118.5 ± 0.37
L750	750	1.5	100	112.4 ± 0.26
L1000	1000	2	100	110.5 ± 0.55
H500	500	1	400	139.4 ± 0.06
H750	750	1.5	400	136.1 ± 0.29
H1000	1000	2	400	127.3 ± 0.35

[a)]Diameter of the frustum base; [b)]Compared to the flat surface area (100%). Data are presented as mean ± SEM.

Furthermore, we calculated the increase in surface area (ΔA) due to pillar dimensions compared to the flat surface:

$$\Delta A = \frac{(R+r)*s*\pi}{p^2}*100 \quad (1)$$

where R is the radius of the pillar top, r the radius of the pillar bottom, s the slope height, and p is the pitch (center-to-center distance). The greatest increase in surface area was calculated on the H500 (39.4% larger than the flat surface area) and was twice the surface area of its corresponding L-array (L500, 18.5% larger than the flat surface area; Table 1).

Water contact angles of flat and nanopillar surfaces were similar: 70 ± 3° and 80 ± 5°, respectively. Nanopillar surfaces were more hydrophobic, possibly due to the increase in surface roughness since surface composition and chemistry of both flat and nanopillar surfaces were identical. All substrates were coated with poly-L-lysine (PLL), which facilitates cell adhesion through unspecific electrostatic interactions without being involved in chemical signaling.[23] After PLL coating, water contact angles decreased to <10° for all substrates. Therefore, the influence of topographical cues on neuronal development was studied in the absence of specific biochemical cues commonly used in cell culture (e.g., laminin, fibronectin).

2.2. Neurons form Paxillin-Rich Adhesions and F-Actin Accumulations on OrmoComp Nanopillars

Both flat and nanopillar OrmoComp substrates supported neuronal growth with no detrimental effects on neuronal cells compared to PLL-coated glass coverslips typically used in neuronal cell culture (Figure S3a, Supporting Information), as previously described in Turunen et al.[22] Moreover, cultures remained stable for long periods of time (DIV16) allowing cortical neurons to form networks (Figure S3b,c, Supporting Information). Neuron-substrate interaction was investigated using scanning electron microscopy and confocal microscopy (**Figure 1**; Figure S4, Supporting Information). Most neurites on L-arrays (100 nm pillar height, Figure 1a; Figure S4a,b, Supporting Information) grew both on the top part of the pillars and on the flat surface between them, while neurites on 400 nm high pillars (H-arrays) were often confined between the pillars and adhered to pillar sidewalls either directly or with filopodial-like processes (Figure 1b,c; Figure S4c,d, Supporting Information). Cured OrmoComp can be considered as a rigid material due to its Young's modulus in GPa range[24] and since the aspect ratio (height/diameter) of all arrays remained relatively small, we did not observe any pillar bending by cellular forces common for softer materials and/or higher aspect ratio structures.[25,26] Investigation of the actin cytoskeleton showed that F-actin accumulated on the nanopillars in the form of ring-like structures visible both in the soma and in larger neurites (Figure 1d,e, arrows). Lou et al.[27] observed that F-actin accumulates at vertical nanostructures and established that the membrane curvature plays a key role in modulating intracellular actin organization and subsequent topography-induced cell signaling and behavior. Furthermore, these formations were often localized with paxillin-rich point contact adhesions (Figure 1d,e,

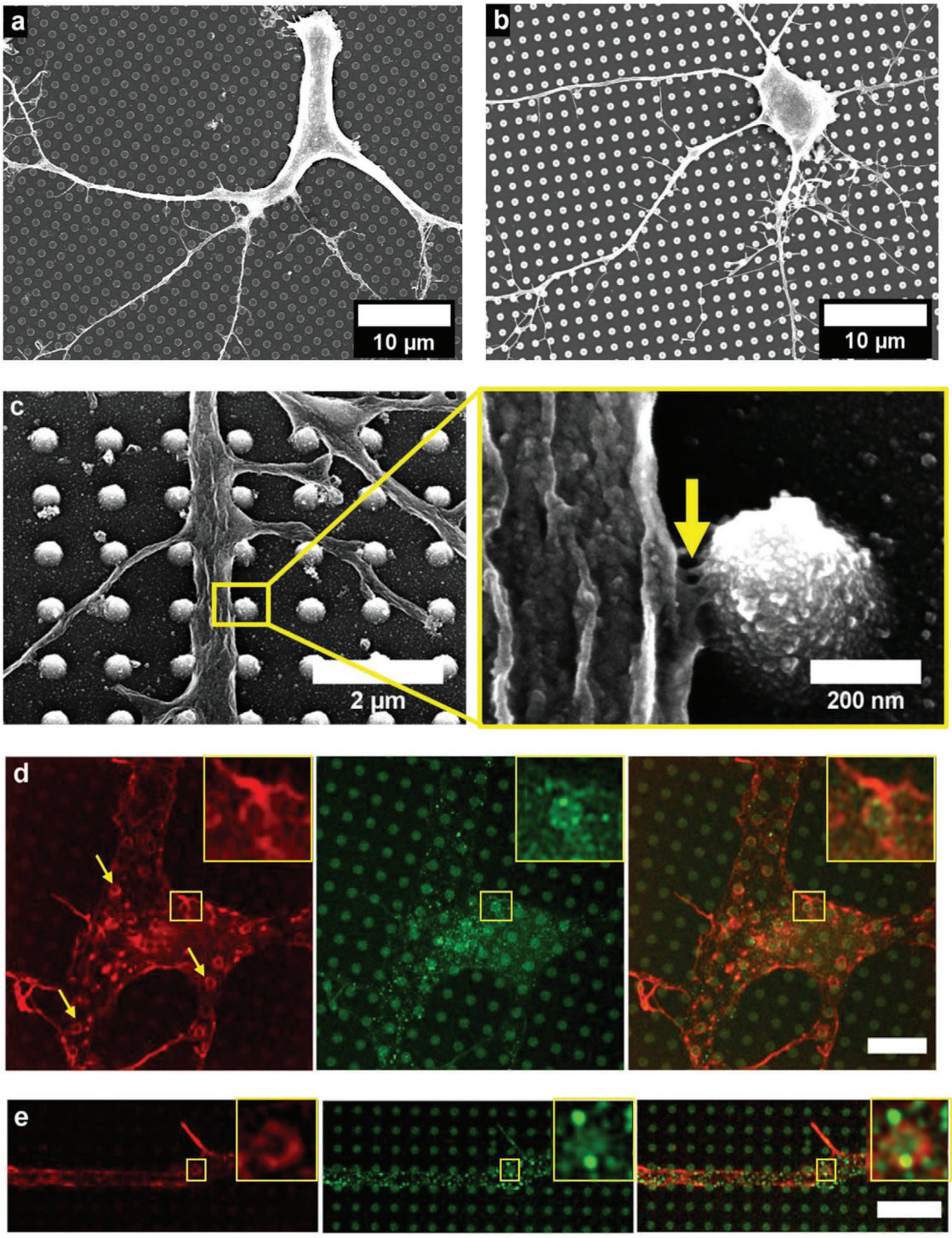

Figure 1. Neuronal growth and adhesion on nanopillar arrays. Neurites extended a) on and between the pillars on L-arrays (100 nm high pillars), while on H-arrays (400 nm high pillars), neurites were mostly confined to the space in b) between the pillars and c) (arrow) adhered to pillar sidewalls. d,e) Nanopillars perturbed the actin cytoskeleton (red) visible by the formation of ring-like structures around the pillars (arrows). These structures were often localized with paxillin-rich point contacts (green; zoomed-in inset). Scale bars: 5 µm.

zoomed-in insets) and could indicate a close contact between the cell membrane and the pillars which is important for improving bioelectronic devices that interface with neurons.[28] Similar formations were not observed on flat substrates and less often on L-arrays (Figure S5a,b, Supporting Information) indicating that higher pillars (400 nm) have a much stronger

effect on the actin cytoskeleton. Neuronal adhesion measured as the soma area was not significantly altered by substrate topography (Figure S5c, Supporting Information).

2.3. Substrate Topography Promotes Axon Development and Growth Cone Elongation

We used time-lapse microscopy to study important aspects of neuronal development in response to substrate topography. Axons in culture differentiated from short processes ≈36 h after plating, then exhibited saltatory growth, cycling between periods of elongation, retraction, and pausing (Movie S1, Supporting Information). We systematically analyzed axonal growth dynamics including the time until axon establishment (initiation time) and the periodicity of cycling between elongation, pausing, and retraction. Cells were allowed to attach to the substrate surface for 5 h before starting time-lapse imaging. After settling and adhering to the substrate, embryonic neurons sprout many thin filopodia (**Figure 2a**, Stage 1, 6 h). Subsequently, immature neurites are formed (Figure 2a, Stage 2, 6–24 h) that go through cycles of growth and retraction without significant net elongation,[29] resulting in a symmetrical morphology of the cell. After ≈24 h in culture, one neurite starts growing rapidly and breaks the overall symmetry, establishes polarity, and becomes the axon (Figure 2a, Stage 3, 24–36 h). Once a neurite exceeds 100 µm, it is likely that it will become an axon.[30,31] Therefore, we measured the time from plating until a neurite exceeds the length of 100 µm (initiation time). Topography significantly accelerated axon establishment on all H-arrays (400 nm height) with an initiation time of 32.2 ± 1.25 h, 32.3 ± 1.35 h, and 32.2 ± 1.36 h on H500, H750, and H1000, respectively, in comparison to the flat surface (41.4 ± 1.83 h, a 20% decrease, Figure 2b). The L500 array (100 nm height) also accelerated axon establishment (33.6 ± 1.30 h), similar to H-arrays, while L750 and L1000 arrays had an average axon establishment time (38.3 ± 1.87 h and 40.2 ± 1.59 h, respectively) similar to the flat surface.

Additionally, time-lapse imaging was used to analyze the effects of topography on axonal growth dynamics that may contribute to earlier axon establishment. Growth cones do not grow steadily: they pause, elongate, and retract and neurons studied in vitro have a similar behavior.[32] Growth cone trajectories were visually analyzed to determine velocity thresholds of elongating, pausing, and retracting events. Growth cone vectors with velocities exceeding 8 µm h^{-1} in the direction of elongation were considered elongating, while those under –8 µm h^{-1} (i.e., in the opposite direction) were considered retracting. Pausing was defined as periods with velocities between 8 and –8 µm h^{-1} followed by an elongation event. For every growth cone, we

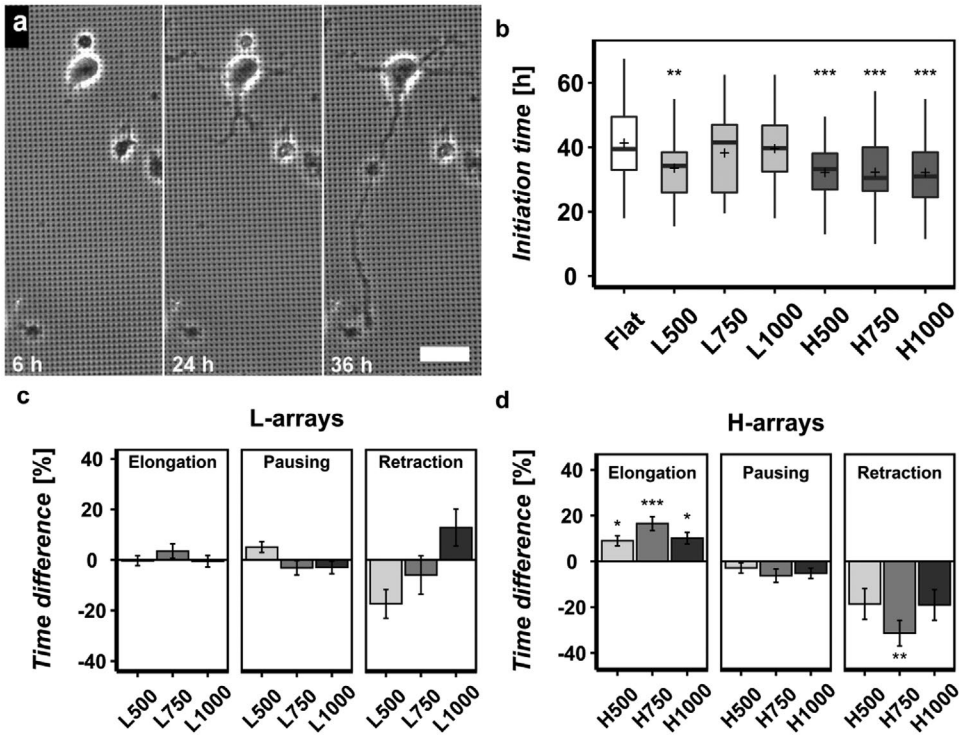

Figure 2. Axon initiation and growth dynamics on nanopillar topographies. a) Several hours after seeding, neurons form many thin filopodia (Stage 1). Subsequently, immature neurites are formed (Stage 2), resulting in a symmetrical cell morphology. Eventually, one neurite starts growing rapidly and breaks the overall symmetry (Stage 3) to become an axon. b) Axon initiation time on nanopillar arrays compared to the flat substrate. Percentage of time growth cones spent elongating, pausing, and retracting normalized to the respective growth phases on the flat substrate c) on L-arrays (100 nm high pillars) and d) on H-arrays (400 nm high pillars). Data in (c) and (d) are presented as mean ± SEM. Number of growth cones tracked: flat = 49, L-arrays (L500 = 58, L750 = 45, L1000, = 55), H-arrays (H500 = 56, H750 = 55, H1000 = 53). Data was compared using the Student's *t*-test with Bonferroni-Holm multiple comparison correction (0.05 significance level). Asterisks indicate a statistically significant difference between flat polymer substrate and nanostructured substrates: * $p < 0.05$, ** $p < 0.01$, *** $p < 0.001$.

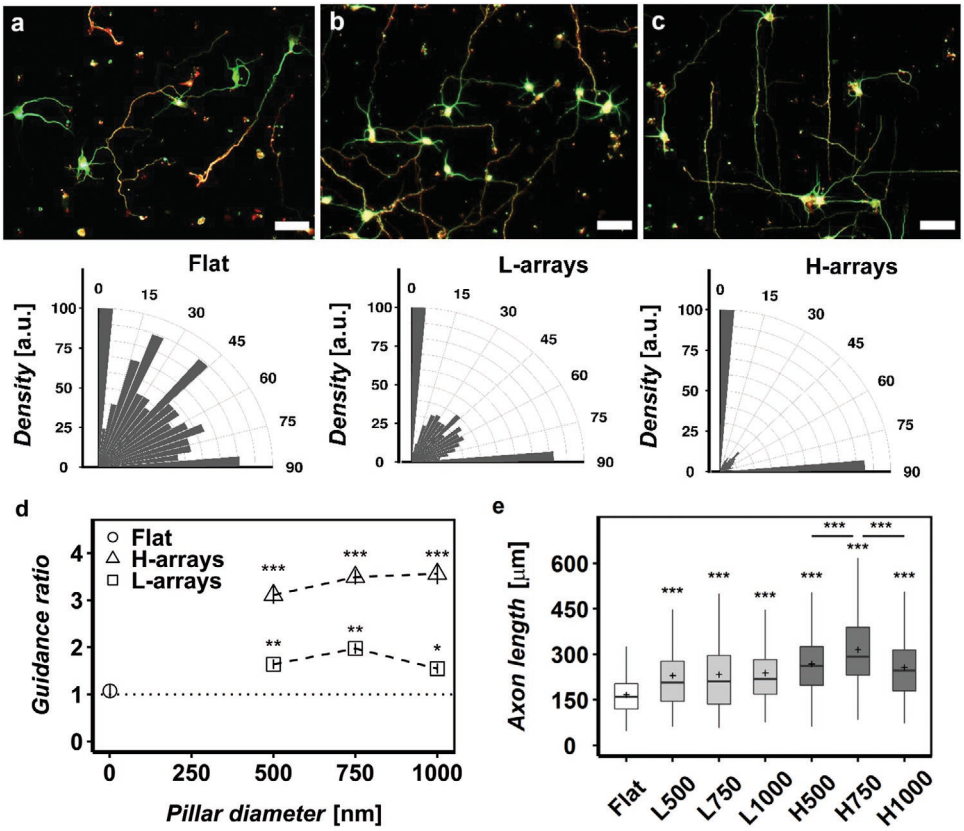

Figure 3. Axon growth and alignment on nanopillar arrays after 3 DIV. Cortical neurons cultured on a) a flat polymer substrate, b) L750 array, and on c) H750 array. Neurons (3 DIV) were fixed and fluorescently labeled for: β-III-tubulin (green), Tau-1 (red). Scale bars: 50 µm. Lower panels represent the distribution of axonal initiation and final angles on flat substrates, L-, and H-arrays. d) Topographical guidance ratio based on initial and final angles on each array compared to the flat substrate. e) Axon lengths. Data was compared using the Student's *t*-test (d) or the Mann–Whitney U test (e) with Bonferroni–Holm multiple comparison correction (0.05 significance level). Asterisks above boxplots without significance bars indicate a statistically significant difference between flat polymer substrate and nanostructured substrates: * $p < 0.05$, ** $p < 0.01$, *** $p < 0.001$.

determined the duration of elongation, pausing, and retraction periods observed during 2 DIV (Figure S6, Supporting Information). The percentage of time spent in each growth phase on nanopillar arrays was normalized to the respective value on a flat substrate. Topography of the L-arrays did not significantly affect the amount of time growth cones spent in periods of growth or nongrowth (pausing and retraction; Figure 2c). Interestingly, growth cones on the L500 array had considerably less retraction events which, although not reaching statistical significance, it concurs with the observed earlier axon establishment on this array (Figure 2b). On the other hand, H-arrays significantly reduced the amount of retraction phases while increasing the amount of elongation phases (Figure 2d). These observations indicate that surface topography significantly affects the axonal growth pattern, especially on higher nanopillars (400 nm), by promoting elongation, reducing retraction, and finally resulting in earlier axon establishment compared to the flat substrate.

2.4. Nanopillars Promote Axon Growth and Alignment to the Topographical Pattern

General morphological features including axon length and topographical alignment were analyzed after 3 DIV, when neurons have defined axons and dendrites.[33] Cortical neurons were fixed and stained with anti-β-III-tubulin (cortical marker) and anti-Tau-1 antibodies (axonal marker) after 3 DIV (**Figure 3**a,b,c). The initial and final axon angles were measured and compared to those on flat substrates (Table S1, Supporting Information). Since the pillars were arranged in a square lattice, axons were considered aligned to the pattern if these angles were 0°, 90°, or 45° (±5°) relative to the direction of the pattern. There were no significant differences between the distributions of initial and final axon angles after 3 DIV meaning that axons tended to align to the topography even under the presumed influence of biochemical signaling from neighboring cells as is typical for later stages of axon growth. Initial and final angles on flat substrates had a random distribution (Figure 3a, lower panel). On the other hand, axons extending on nanopillar arrays grew along the topographical pattern. Angle distributions on 400 nm high pillars (H-arrays) showed the strongest peaks centered on 0° and 90°, indicating that a large fraction of axons did not deviate from topographically dictated angles (Figure 3c, lower panel). Axons were far less aligned along the diagonal direction (45°), that is, neurites tended to predominantly extend to the nearest possible pillar (center-to-center distance of n) and very rarely to the second nearest pillar ($\sqrt{2}n$). Distributions on pillars with 100 nm height (L-arrays) had larger peaks around the

topographically non-dictated angles indicating greater variability in axon alignment on lower pillars (Figure 3b, lower panel).

Furthermore, axon alignment was quantified by calculating the ratio of the number of aligned axons (0°, 45°, 90°; ±5°) and the number that would be expected in a uniform distribution without guidance cues, that is, on a flat surface (guidance ratio [GR]). All nanopillar arrays had a significantly higher guidance ratio compared to the flat substrate with H-arrays having significantly higher guidance ratios than the L-arrays (Figure 3d). No significant differences were observed in relation to different pillar diameters. These results suggest that topographic alignment is primarily sensitive to the height of the underlying pillar patterns possibly due to neurite confinement between the nanopillars (Figure 1c). Torre et al.[34] showed that growth cones and neurites easily crawl over 100 nm high obstacles but less frequently over those higher than 300 nm. If we assume that higher pillars constrain axon growth only along the topographical pattern, then neurites that initiate and start growing along the pattern could have a higher probability to develop into axons than unaligned neurites.

All topographies promoted axon growth, resulting in neurons having longer axons compared to those on the flat polymer substrate (Figure 3e). Neurons on H750 array had the longest axons after 3 DIV compared to other arrays. Kang et al.[35] observed a similar behavior with 670 nm silica beads inducing the highest neurite lengths. Neurons had an increase in median axon length of ≈40% on H-arrays (400 nm high pillars) in comparison to the flat substrate and a ≈20% increase compared to their corresponding 100 nm high counterparts (L-arrays, Figure 3e). Chua et al.[36] demonstrated that neurite elongation, alignment, and neuronal differentiation were increased with increasing depth of gratings. Similarly, our results show that increasing the pillar aspect ratio 4 times (height/diameter), leads to considerable changes in growth dynamics of extending axons, that is, more elongation and less retraction phases, resulting in longer axons (Figure 2d, Figure 3e).

2.5. Nanopillars Increase the Number of Point Contact Adhesions in the Growth Cone and Reduce F-Actin Retrograde Flow Rates

Growth cones, much like motile cells, must exert a force on the substrate to generate traction and move forward. Traction forces on the substrate are localized within the growth cone's actin-rich peripheral domain.[37] Numerous filopodia protruding from the peripheral domain explore the environment and adhere to the substrate through point contact adhesions.[38] These adhesions, coupled with the rapid assembly of actin filaments and myosin which together generate the retrograde flow of F-actin, facilitate the transmission of actomyosin activity onto the substrate in the form of traction forces. Nanopillar topographies present a larger surface area (Table 1) and more adhesion opportunities to anchor the growth cone's filopodia. Therefore, neurons (DIV3) were fixed and labeled with the anti-paxillin antibody and

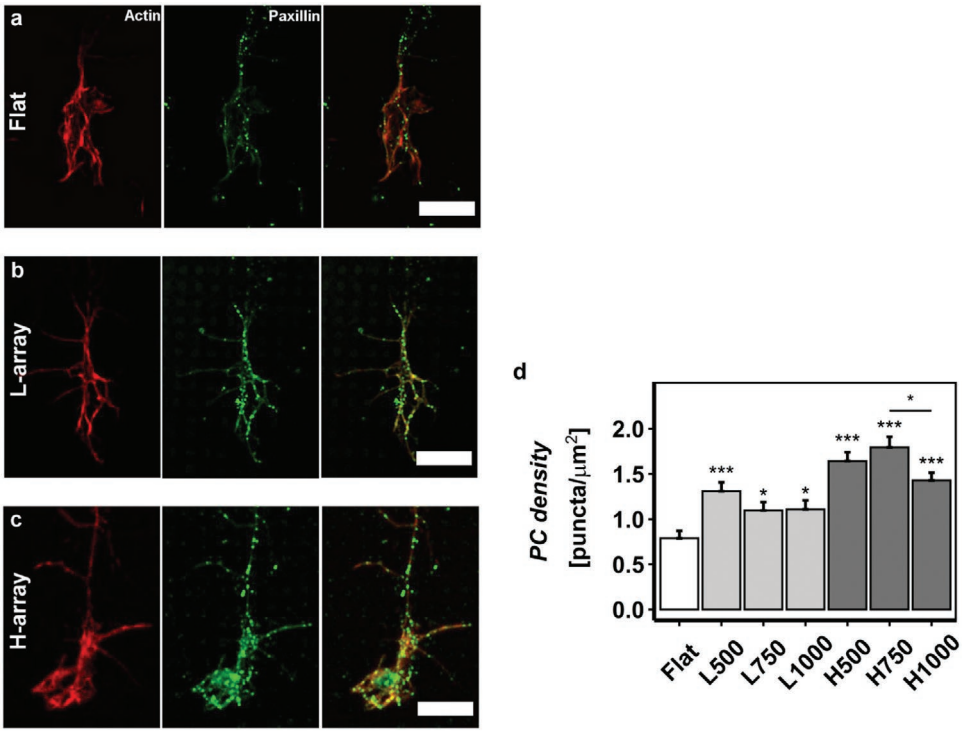

Figure 4. Growth cone point contacts on nanopillar arrays at 3 DIV. Representative images of growth cones cultured on a) a flat substrate, b) L750 array, and on c) H750 array. Growth cones were fluorescently labeled for: F-actin (TRITC-phalloidin, red) and paxillin (anti-paxillin antibody, green). Scale bars: 5 μm. d) Quantification of the number of paxillin puncta normalized to the growth cone area. Number of growth cones analyzed: flat = 29, L-arrays (L500 = 19, L750 = 15, L1000, = 13), and H-arrays (H500 = 17, H750 = 24, H1000 = 28). Data in (d) is presented as mean ± SEM. Data was compared using the Student's *t*-test with Bonferroni–Holm multiple comparison correction (0.05 significance level). Asterisks indicate a statistically significant difference between flat substrate and nanostructured substrates: * $p < 0.05$, ** $p < 0.01$, *** $p < 0.001$.

TRITC-phalloidin to visualize paxillin-rich point contact adhesion and the F-actin cytoskeleton, respectively (**Figure 4**a–c). Paxillin puncta were localized both in the growth cone's central domain as well as in filopodia. Moreover, we observed significantly more paxillin puncta in growth cones on nanopillars compared to the flat substrate. The number of paxillin point contacts was quantified and normalized to the growth cone area obtained using a thresholded mask of the actin signal (Figure 4d). We observed that growth cones on nanopillar arrays form significantly more point contacts in comparison to the flat substrate. Furthermore, growth cones on H-arrays had considerably more paxillin puncta in comparison to L-arrays ($p = 0.00004$), corresponding to their higher surface area provided by pillar sidewalls.

A higher adhesion density has been linked to a slower retrograde flow.[39] Moreover, Nichol et al.[40] showed that the assembly of new point contact adhesions is temporally and spatially linked to the reduction of F-actin retrograde flow rates at sites of forward membrane protrusion and several studies suggested that local reductions in retrograde flow are correlated with increased growth cone motility[41,42] and its movement toward areas of strong adhesion.[43] Evidence of similar mechanisms were recently found during contact guidance in vivo.[44] Therefore, we evaluated the F-actin retrograde flow in growth cones on nanopillar arrays. A slower actin retrograde flow indicates a stronger molecular clutch through increased number of adhesion points. Cortical neurons were transfected with a fluorescent F-actin marker (Lifeact-RFP) and imaged using high-resolution time-lapse microscopy. Each Lifeact-RFP-expressing growth cone was imaged for 2.5–5 min in 2–3 s intervals and 1-pixel line kymographs were generated from different regions of the growth cone (**Figure 5**a). The slopes of the generated kymographs were used to calculate retrograde flow velocities with higher slopes indicating a slower flow rate (Figure 5b, arrows). We observed that nanopillars induced a reduction in the average actin retrograde flow rates (Figure 5c) in relations similar to the increase in point contact density (Figure 4d) with the largest decrease found on H-arrays.

These results indicate that increased surface area available to the growth cone on nanopillar arrays leads to increased assembly of paxillin-rich point contact adhesions in the growth cone and a reduction in F-actin retrograde flow rates (Figure 5d). Therefore, the observed accelerated outgrowth, along with promotion of growth cone elongation on higher pillars could result from the increased surface area provided by the sloped pillar sidewalls (slope angle 120°) that is available for growth cone coupling. Additionally, a certain level of roughness provided by nanoscale grooves and ridges on pillar sidewalls (Figure S2c, Supporting Information) could

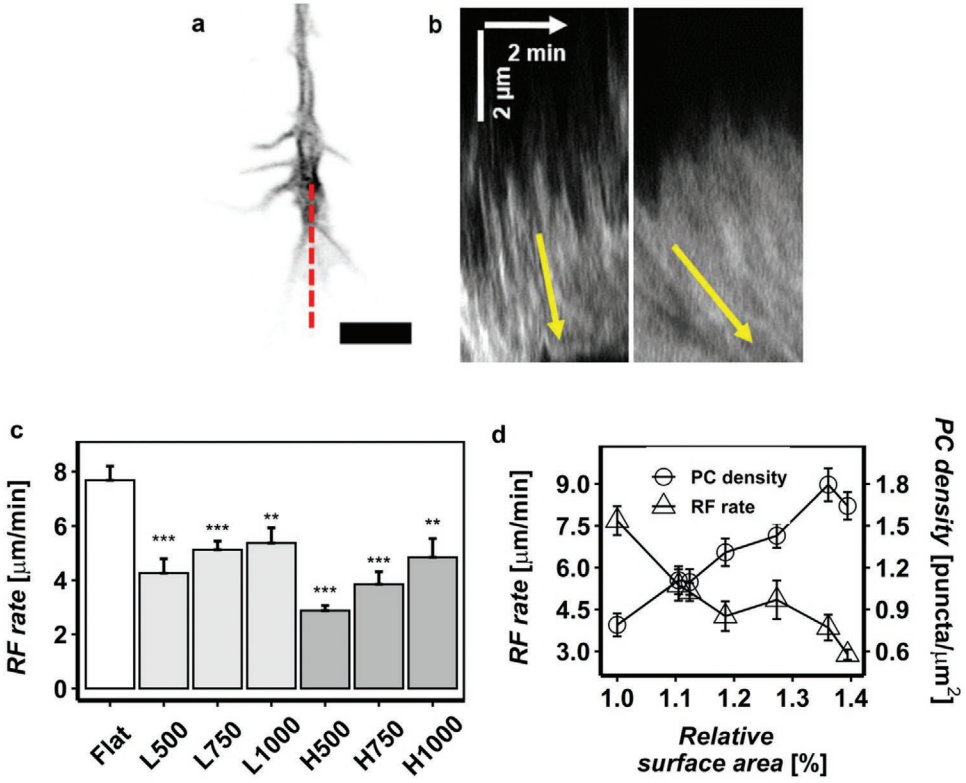

Figure 5. F-actin retrograde flow rates on nanopillar arrays at 3 DIV. a) A Lifeact-RFP-expressing growth cone including an exemplary kymograph line scan (dashed red). b) Representative actin kymographs generated from 5 min time-lapse videos (2.5 sec interval). Arrows indicate the slopes used to calculate flow rates. c) Average actin retrograde flow rate on different substrates. Number of growth cones analyzed: flat = 26, L-arrays (L500 = 8, L750 = 11, L1000, = 8), and H-arrays (H500 = 21, H750 = 9, H1000 = 5). d) Increase in surface area on nanopillar arrays (Table 1) relative to the flat substrate (denoted as 1) leads to increased paxillin adhesion density and a reduction in F-actin retrograde flow rates. Data in c) and d) is presented as mean ± SEM. Data was compared using the Student's *t*-test with Bonferroni–Holm multiple comparison correction (0.05 significance level). Asterisks indicate a statistically significant difference between flat substrate and nanostructured substrates: * $p < 0.05$, ** $p < 0.01$, *** $p < 0.001$.

also contribute to increased neurite adhesion on pillar sidewalls. Neurites are more likely to adhere strongly to structures possessing grooves and ridges than to smooth surfaces.[45] Furthermore, higher pillars acted as stronger angular constraints by confining neurite outgrowth along the topographical pattern (Figure 3d) leading to an assembly of point contact adhesions on pillar sidewalls thus creating the greatest traction forces to preferentially extend the neurites between the pillars (Figure 1e, arrow). This effect was weaker on 100 nm high pillars since they could not constrain neurite outgrowth of as much as 400 nm high pillars.

3. Conclusion

In conclusion, we demonstrate that OrmoComp nanopillar arrays represent a cost-efficient and reproducible platform for studying nanotopographical modulation of neuronal development. Cortical neurons formed close contact with the nanoscale pillars as manifested by the assembly of adhesions and F-actin accumulations around the pillars. This is especially relevant for bioelectronic devices to ensure optimal communication between the device and living tissue. Furthermore, nanopillars promoted axon growth and alignment to the topographical pattern resulting in longer axons compared to flat substrates. A larger surface area presented by the nanopillars induced increased assembly of point contact adhesions in the growth cone and a reduction in actin retrograde flow rates allowing for growth cone elongation. These findings highlight the importance of the surface area provided by highly ordered nanotopographies for stronger growth cone coupling and subsequent neurite outgrowth. We believe that this work along with further research into specific molecular mechanisms during distinct events of axonal development could be useful for guiding novel designs of neural interfaces in tissue engineering and bioelectronics.

4. Experimental Section

Fabrication and Surface Modification of Si/SiO_2 Molds: Si/SiO_2 molds were fabricated on 4-inch silica wafers (n-type, 500–550 µm thickness, <100> crystal orientation, 2–10 Ωcm volume resistivity, Si-Mat company) using a top-down approach (Figure S1, Supporting Information). Wafers were oxidized to obtain a SiO_2 layer with a thickness of 100 and 500 nm to fabricate molds with 100 nm pit depth and 400 nm pit depth, respectively. A layer of polymethylmethacrylate resist (PMMA, AR-P 669.04, Allresist) was deposited homogeneously on the wafer using spin coating and the nanopatterns were transferred onto the resist using electron beam lithography (EBL, EBPG 5000plus from Vistec B.V., now Raith B.V.). The wafers were then immersed in developer AR600-55 (Allresist) to remove soluble PMMA fragments created by the electron beam and dipped in isopropanol (Sigma-Aldrich) to stop the developer effect. Finally, nanopits of specified dimensions were etched into the exposed SiO_2 using reactive ion etching (CH_3/SF_6 plasma chemistry; RIE, Oxford Instruments). The development time and the RIE process were adapted according to the thickness of the resist and etching depth. The mold surface cleaned with oxygen plasma and passivated using trichloro(1H, 1H, 2H, 2H-perfluorooctyl)silane (FOTCS, Sigma-Aldrich) to facilitate polymer removal after the replication process. The FOTCS molecules interact covalently with —OH groups on the surface, which increases the surface hydrophobicity, thereby inducing a repellent behavior.

Fabrication of OrmoComp Replicas: OrmoComp polymer was deposited on quartz 4-inch wafers (Plan Optics AG). The wafers were first coated with OrmoPrime and baked at 150 °C to promote polymer adhesion followed by OrmoComp deposition by spin coating. The quartz/OrmoComp replicas were produced using nanoimprint lithography (NIL, NX-2000, Nanonex Corp). The mold and the quartz/OrmoComp wafer were placed together and compressed by an air cushion method at 500 psi (34.5 bar), followed by UV curing (Figure S2, Supporting Information). Before cell seeding, the substrates were sterilized by briefly dipping them in 70% ethanol and dried with N_2 gas. Substrates were coated with 1% PLL (1 µg mL^{-1} in sterile H_2O, Sigma-Aldrich) in HBSS for 1 h at room temperature. Wells were washed once with an equal volume of HBSS and stored at 4 °C.

Primary Cell Culture: All animal experiments were done in accordance with the EU Directive 2010/63/EU for animal experiments and Landesumweltamt für Natur, Umwelt und Verbraucherschutz Nordrhein-Westfalen, Recklinghausen, Germany; and approved by Landesumweltamt für Natur, Umwelt und Verbraucherschutz Nordrhein-Westfalen (84-02.04.2015.A173 and 81-02.04.2018.A190). Primary cortical neurons were isolated from E18 rat embryos of either sex by trypsinization followed by mechanical trituration. Pregnant Wistar female rats were acquired from Charles River Laboratories (Sulzfeld, Germany) and handled by a certified technician. Dissociated cells were suspended in Neurobasal medium (Life Technologies) supplemented with 1% (vol/vol) B-27 (Invitrogen), GlutaMAX (0.5 mM, Invitrogen), and gentamycin antibiotic (50 µg mL^{-1}). Additionally, a fluorescent F-actin marker Lifeact-RFP was introduced to visualize actin dynamics.[46] Transfection with Lifeact-RFP plasmid was done using the Amaxa Rat Neuron Nucleofector Kit (program G-013; Lonza). Cells were seeded on PLL-coated substrates at a density of 150 cells/mm^2. After settling at RT for 10 min, cultures were transferred to an incubator (5% CO_2, 37 °C, 100% humidity), and the medium was replaced after 2 h.

Long-Term Time-Lapse Microscopy: Time-lapse images of axonal outgrowth were acquired every 30 min for 46 h starting from 5 h after plating. Experiments were performed using an Axio Observer.Z1 (Zeiss) inverted microscope equipped with an incubation chamber (PeCon) with a temperature, CO_2, and humidity control. Additionally, the setup was equipped with a Colibri fluorescence system (Zeiss) and a PCO.edge 5.5 sCMOS camera. All images were acquired using a 40× air objective (LD Plan-Neofluar, 0.6 NA, Ph2, Zeiss). Time-lapse sequences were processed using Fiji software.[47] Briefly, the sequences were stabilized to correct for sample drift in the xy-plane during imaging using Fiji's StackReg plugin.[48] The axon growth was traced back manually using the MTrackJ plugin[49] whereby only the longest neurite or branch was measured. Actual axonal length in each time interval was estimated from growth cone trajectories by adding each displacement that moved away from the soma (elongation) to the axon length and subtracting those that moved toward the soma (retraction). This method provided accurate estimates of axonal length provided that the axons did not make sharp turns. Growth cones from 3 independent culture dishes for each substrate were analyzed and the data was processed using R software.

Analysis of F-Actin Retrograde Flow in Growth Cones: High-resolution time-lapse images of Lifeact-RFP-expressing growth cones were imaged using a 63× oil immersion objective (Plan-Apochromat, 1.4 NA, Zeiss) on a confocal laser-scanning microscope Axio Observer LSM 880 equipped with an Airyscan detector providing super-resolution imaging with increased acquisition speeds. Growth cones were imaged for 2.5–5 min in 2–3 s intervals with an optical zoom of 2.5–3×. Kymographs were produced using Fiji's Multiple kymograph plugin. 1-pixel-wide lines were drawn perpendicular to the GC leading edge and assembled into a kymograph representation where time is measured along the *y*-axis in seconds, with 2–3 seconds between each line depending on acquisition rate. Each growth cone was sampled with 6–10 lines and the slopes of the resulting diagonal patterns appearing in the kymograph were used to calculate the actin retrograde flow rate.

Fluorescent Immunocytochemistry: Neuronal cell morphology and individual cell components such as axons and dendrites were visualized using fluorescent immunocytochemistry. After 3 DIV, the cells were fixed with 4% paraformaldehyde (Sigma-Aldrich) diluted in PBS for 10 min at RT and permeabilized with 0.3% Triton X-100 (Sigma-Aldrich) in blocking buffer (BB, 2% bovine serum albumin and 2% heat-inactivated goat serum diluted in PBS, Sigma-Aldrich) for 15 min at RT. Unspecific binding sites were blocked with BB at 4 °C in the dark overnight. Afterwards, substrates were rinsed and incubated with primary antibodies. Primary antibodies against β-III-tubulin (cortical marker; 1 µg mL^{-1}, rabbit-T2200, Sigma-Aldrich) and Tau-1 (axonal marker; 4 µg mL^{-1}, mouse-PC1C6, Sigma-Aldrich). The secondary antibodies used were goat anti-rabbit Alexa Fluor 488 (Life Technologies) and goat anti-mouse Alexa Fluor 633 (Life Technologies) both diluted to 4 µg mL^{-1} in BB. Cell nuclei were visualized with 4′,6-diamidin-2-phenylindol (DAPI, Sigma-Aldrich). Fluorescence microscopy was performed using a 20× objective (EC Plan-Neofluar, 0.5 NA, Zeiss) and analyzed using Fiji's NeuronJ plugin[50] to obtain cell viability, neurite length, axonal initial and final angles, and soma area. Neurons that formed clusters were not included in the analysis. Fluorescent images were oriented with the grid of structures aligned to vertical and horizontal axes and angles were measured with respect to the direction of the pattern. Axon length and orientation were measured using images of Tau-1 axon-specific staining of single neurons. The initial angle was measured before the first change in axon direction and the last angle of the axon was measured as the final path finding angle. The axon turns between the initial and final angles were not considered. Since the topographical pattern had a fourfold rotational symmetry, the guidance ratio for specific topographically dictated angles was defined by taking a region of 10° centered on the considered angles (i.e., 0° ± 5°, 90° ± 5°, and 45° ± 5°). The number of axons whose initial and final angles were within this region (N_{aligned}) was calculated and normalized to the number of axons that would be expected to have angles in these regions in a uniform distribution (Equation 2), that is, in the absence of topographical cues (N_{uniform}).

$$\text{GR} = \frac{N_{\text{aligned}}}{N_{\text{uniform}}} \tag{2}$$

More than 200 cells from at least 3 independent culture dishes for each substrate were analyzed and the data processed using R software.

Point contact adhesions were visualized using the anti-paxillin antibody [Y113] (2 µg mL^{-1}, ab32084, Abcam) followed by incubation with goat anti-rabbit Alexa Fluor 488 secondary antibody (4 µg mL^{-1}, Life Technologies). Cells were additionally stained with TRITC-phalloidin (2.5 µg mL^{-1} Sigma Aldrich) to visualize the actin cytoskeleton. Images were acquired with a 63× oil immersion objective (Plan-Apochromat, 1.4 NA, Zeiss) on a confocal laser-scanning microscope LSM 880 equipped with an Airyscan detector and processed to enhance the individual paxillin puncta.[51] The number of puncta was quantified using the Fiji's particle analyzer and normalized to the growth cone area outlined from thresholded images of TRITC-phalloidin (actin) signal.

Scanning Electron Microscopy (SEM): Alternatively, cells were fixed with 3.2% glutaraldehyde (Sigma) in PBS. After fixation, samples were dehydrated in increasing concentrations of ethanol: 10%, 30%, 50%, 70%, 90%, and 95% (vol/vol). The samples were then stored in 100% ethanol. Samples were prepared using either critical point drying (CPD 030, BAL-TEC Company) or resin embedding method[52] and metalized with a thin layer of Ir (5 nm). SEM images were made from the top or with a 45° or 52° tilt angle using the SE detector and beam acceleration of 3–10 kV (1550VP, Zeiss and Helios 600i Nanolab Dual-beam, FEI).

Statistical Analysis: Data was analyzed and plots produced using R software (version 3.4.1). Quantitative measurements were analyzed via a Shapiro–Wilk test to assess normality and then compared using the nonparametric Mann–Whitney *U*-test or the parametric Student's *t*-test. Multiple comparisons correction was done using the Holm–Bonferroni method. All boxplots are Tukey type with the median denoted as a line and the mean as a black cross. A *p*-value less than 0.05 was considered statistically significant.

Supporting Information

Supporting Information is available from the Wiley Online Library or from the author.

Acknowledgements

The authors kindly thank Bettina Breuer, Regina Stockmann, and Michael Prömpers for technical support. Elke Reuters-Brauweiler, Elmar Neumann, and Pegah Shokoohimehr are appreciated for SEM preparation and investigation.

Open access funding enabled and organized by Projekt DEAL.

Conflict of Interest

The authors declare no conflict of interest.

Keywords

axon growth, F-actin dynamics, growth cones, nanotopographies, point contact adhesions, polymer nanopillars

Received: September 2, 2020
Published online: January 14, 2021

[1] K. H. Nakayama, L. Hou, N. F. Huang, *Adv. Healthcare Mater.* **2014**, *3*, 628.
[2] D. E. Jaalouk, J. Lammerding, *Nat. Rev. Mol. Cell Biol.* **2009**, *10*, 63.
[3] P. P. Provenzano, D. R. Inman, K. W. Eliceiri, S. M. Trier, P. J. Keely, *Biophys. J.* **2008**, *95*, 5374.
[4] K. M. Yamada, E. Cukierman, *Cell* **2017**, *130*, 601.
[5] J. A. Kshitiz, S. Y. Kim, D. H. Kim, *Cell Adhes. Migr.* **2015**, *9*, 300.
[6] A. Rajnicek, S. Britland, C. McCaig, *J. Cell Sci.* **1997**, *110*, 2905.
[7] F. Haq, V. Anandan, C. Keith, G. Zhang, *Int. J. Nanomed.* **2007**, *2*, 107.
[8] V. Chaurey, F. Block, Y. H. Su, P. C. Chiang, E. Botchwey, C. F. Chou, N. S. Swami, *Acta Biomater.* **2012**, *8*, 3982.
[9] S. Seyock, V. Maybeck, E. Scorsone, L. Rousseau, C. Hébert, G. Lissorgues, P. Bergonzo, A. Offenhäusser, *RSC Adv.* **2017**, *7*, 153.
[10] D. Y. Fozdar, J. Y. Lee, C. E. Schmidt, S. Chen, *Int. J. Nanomed.* **2011**, *6*, 45.
[11] A. Belu, M. Yilmaz, E. Neumann, A. Offenhäusser, G. Demirel, D. Mayer, *J. Biomed. Mater. Res., Part A* **2018**, *106*, 1634.
[12] B. Nadarajah, P. Alifragis, R. O. L. Wong, J. G. Parnavelas, *Nat. Neurosci.* **2002**, *5*, 218.
[13] R. P. Bunge, *J. Neurol.* **1994**, *242*, S19.
[14] A. M. Avellino, D. Hart, A. T. Dailey, M. MacKinnon, D. Ellegala, M. Kliot, *Exp. Neurol.* **1995**, *136*, 183.
[15] C. E. Schmidt, J. B. Leach, *Annu. Rev. Biomed. Eng.* **2003**, *5*, 293.
[16] A. Blau, *Curr. Opin. Colloid Interface Sci.* **2013**, *18*, 481.
[17] E. W. Keefer, B. R. Botterman, M. I. Romero, A. F. Rossi, G. W. Gross, *Nat. Nanotechnol.* **2008**, *3*, 434.
[18] S. Qi, C. Yi, S. Ji, C. C. Fong, M. Yang, *ACS Appl. Mater. Interfaces* **2009**, *1*, 30.
[19] J. T. Robinson, M. Jorgolli, A. K. Shalek, M. H. Yoon, R. S. Gertner, H. Park, *Nat. Nanotechnol.* **2012**, *7*, 180.
[20] C. Xie, Z. Lin, L. Hanson, Y. Cui, B. Cui, *Nat. Nanotechnol.* **2012**, *7*, 185.
[21] E. Käpylä, A. Sorkio, S. Teymouri, K. Lahtonen, L. Vuori, M. Valden, H. Skottman, M. Kellomäki, K. Juuti-Uusitalo, *Langmuir* **2014**, *30*, 14555.

[22] S. Turunen, T. Joki, M. L. Hiltunen, T. O. Ihalainen, S. Narkilahti, M. Kellomäki, *ACS Appl. Mater. Interfaces* **2017**, *9*, 25717.
[23] P. Li, K. Greben, R. Wördenweber, U. Simon, A. Offenhäusser, D. Mayer, *RSC Adv.* **2015**, *5*, 39252.
[24] C. Schizas, D. Karalekas, *J. Mech. Behav. Biomed. Mater.* **2011**, *4*, 99.
[25] J. Fu, Y. K. Wang, M. T. Yang, R. A. Desai, X. Yu, Z. Liu, C. S. Chen, *Nat. Methods* **2010**, *7*, 733.
[26] N. D. Evans, E. Gentleman, *J. Mater. Chem. B* **2014**, *2*, 2345.
[27] H. Y. Lou, W. Zhao, X. Li, L. Duan, A. Powers, M. Akamatsu, F. Santoro, A. F. McGuire, Y. Cui, D. G. Drubin, B. Cui, *Proc. Natl. Acad. Sci. USA* **2019**, *116*, 23143.
[28] L. Hanson, Z. C. Lin, C. Xie, Y. Cui, B. Cui, *Nano Lett.* **2012**, *12*, 5815.
[29] C. G. Dotti, C. A. Sullivan, G. A. Banker, *J. Neurosci.* **1988**, *8*, 1454.
[30] A. Sakakibara, Y. Hatanaka, *Front. Neurosci.* **2015**, *9*, 116.
[31] Y. Hatanaka, K. Yamauchi, *Cereb. Cortex* **2013**, *23*, 105.
[32] V. Argiro, M. B. Bunge, M. I. Johnson, *J. Neurosci.* **1984**, *4*, 3051.
[33] N. Arimura, K. Kaibuchi, *Nat. Rev. Neurosci.* **2007**, *8*, 194.
[34] T. L. Lien, J. Ban, M. Tormen, E. Migliorini, G. Grenci, A. Pozzato, V. Torre, *PLoS One* **2013**, *8*, e73966.
[35] K. Kang, S.-E. Choi, H. S. Jang, W. K. Cho, Y. Nam, I. S. Choi, J. S. Lee, *Angew. Chem., Int. Ed. Engl.* **2012**, *51*, 2855.
[36] J. S. Chua, C. P. Chng, A. A. K. Moe, J. Y. Tann, E. L. K. Goh, K. H. Chiam, E. K. F. Yim, *Biomaterials* **2014**, *35*, 7750.
[37] C. Hyland, A. F. Mertz, P. Forscher, E. Dufresne, *Sci. Rep.* **2014**, *4*, 4617.
[38] S. Woo, *J. Neurosci.* **2006**, *26*, 1418.
[39] D. Koch, W. J. Rosoff, J. Jiang, H. M. Geller, J. S. Urbach, *Biophys. J.* **2012**, *102*, 452.
[40] R. H. Nichol, K. M. Hagen, D. C. Lumbard, E. W. Dent, T. M. Gomez, *J. Neurosci.* **2016**, *36*, 2267.
[41] C. H. Lin, P. Forscher, *Neuron* **1995**, *14*, 763.
[42] C. H. Lin, E. M. Espreafico, M. S. Mooseker, P. Forscher, *Neuron* **1996**, *16*, 769.
[43] D. M. Suter, L. D. Errante, V. Belotserkovsky, P. Forscher, *J. Cell Biol.* **1998**, *141*, 227.
[44] T. Minegishi, Y. Uesugi, N. Kaneko, W. Yoshida, K. Sawamoto, N. Inagaki, *Cell Rep.* **2018**, *25*, 624.
[45] T. Limongi, F. Cesca, F. Gentile, R. Marotta, R. Ruffilli, A. Barberis, M. Dal Maschio, E. M. Petrini, S. Santoriello, F. Benfenati, E. Di Fabrizio, *Small* **2013**, *9*, 402.
[46] J. Riedl, A. H. Crevenna, K. Kessenbrock, J. H. Yu, D. Neukirchen, M. Bista, F. Bradke, D. Jenne, T. A. Holak, Z. Werb, M. Sixt, R. Wedlich-Soldner, *Nat. Methods* **2008**, *5*, 605.
[47] J. Schindelin, I. Arganda-Carreras, E. Frise, V. Kaynig, M. Longair, T. Pietzsch, S. Preibisch, C. Rueden, S. Saalfeld, B. Schmid, J.-Y. Tinevez, D. J. White, V. Hartenstein, K. Eliceiri, P. Tomancak, A. Cardona, *Nat. Methods* **2012**, *9*, 676.
[48] P. Thevenaz, U. E. Ruttimann, M. Unser, *IEEE Trans. Image Process.* **1998**, *7*, 27.
[49] E. Meijering, O. Dzyubachyk, I. Smal, *Methods Enzymol.* **2012**, *504*, 183.
[50] E. Meijering, M. Jacob, J.-C. F. Sarria, P. Steiner, H. Hirling, M. Unser, *Cytometry, Part A* **2004**, *58A*, 167.
[51] U. Horzum, B. Ozdil, D. Pesen-Okvur, *MethodsX* **2014**, *1*, 56.
[52] A. Belu, J. Schnitker, S. Bertazzo, E. Neumann, D. Mayer, A. Offenhaeusser, F. Santoro, *J. Microsc.* **2016**, *263*, 78.